molecules

MDPI

*Article*

# pH and Salt-Assisted Macroscopic Chirality Inversion of Gadolinium Coordination Polymer

**Ting Hou [1], Lan-Qing Wu [1], Yan Xu [1,2], Song-Song Bao [1] and Li-Min Zheng [1,*]**

[1] State Key Laboratory of Coordination Chemistry, School of Chemistry and Chemical Engineering, Collaborative Innovation Center of Advanced Microstructures, Nanjing University, Nanjing 210023, China
[2] Institute of Information Engineering, Suqian College, Suqian 223800, China
* Correspondence: lmzheng@nju.edu.cn

**Abstract:** The precise adjustment of handedness of helical architectures is important to regulate their functions. Macroscopic chirality inversion has been achieved in organic supramolecular systems by pH, metal ions, solvents, chiral and non-chiral additives, temperature, and light, but rarely in coordination polymers (CPs). In particular, salt-assisted macroscopic chirality inversion has not been reported. In this work, we carried out a systematic investigation on the role of pH and salt in regulating the morphology of CPs based on $Gd(NO_3)_3$ and *R*-(1-phenylethylamino)methylphosphonic acid (*R*-pempH$_2$). Without extra $NO_3^-$, the chirality inversion from the left-handed superhelix ***R*-M** to the right-handed superhelix ***R*-P** can be achieved by pH modulation from 3.2 to 3.8. The addition of $NaNO_3$ (2.0 eq) at pH 3.8 results in an inversion of chiral sense from ***R*-P** to ***R*-M** as a pure phase. To our knowledge, this is the first example of salt-assisted macroscopic helical inversion in artificial systems.

**Keywords:** coordination polymers; salt-assisted; chirality inversion



**Citation:** Hou, T.; Wu, L.-Q.; Xu, Y.; Bao, S.-S.; Zheng, L.-M. pH and Salt-Assisted Macroscopic Chirality Inversion of Gadolinium Coordination Polymer. *Molecules* **2023**, *28*, 163. https://doi.org/10.3390/molecules28010163

Academic Editor: Afang Zhang

Received: 23 November 2022
Revised: 17 December 2022
Accepted: 20 December 2022
Published: 25 December 2022



## 1. Introduction

Helical architectures are ubiquitous in nature and display unique functions and topological properties [1–4]. Due to the uncertainty of chiral transcription and translation, the induction and inversion of helical structures is one of the most complex processes in biological systems [5]. Therefore, achieving multi-level assembly of helical structures from molecular to macroscopic levels in artificial systems with controllable macroscopic helical sense and elucidating the underline mechanism have become one of the hot spots in the research of chiral materials [6]. To date, the study of modulating the helical sense of the macroscopic helical structures via external stimuli has received increasing attention. Chiral inversion that can be achieved by pH [7–12], metal ions [13–18], solvents [19–24], chiral and non-chiral additives [25–32], temperature [33,34], light [35,36] have been reported, which are often associated with the modulation of non-covalent interactions, such as hydrogen bonds, van der Waals forces, and electrostatic interactions. However, it is worth noting that salt-mediated modulation of the chiral sense of helical structures has not been reported.

Salt plays an important role in living systems. Moderate salt intake can alleviate or prevent some diseases and improve body functions [37–39]. In addition, salt can alter non-covalent interactions, which may affect the self-assembly process. For example, high concentrations of salt can modulate the strength of electrostatic interactions between charged groups, destroy hydrogen bonds in protein secondary structure, cause changes of the α-helix [40,41] and β-sheet [42,43], or disrupt the structure of DNA, leading to structural changes from Z-DNA to Z′-DNA, or B-DNA to Z-DNA [44]. Various salts can also be used as additives to control the size, morphology, structure of inorganic crystals [45–49]. However, salt has rarely been used to control the morphology and structure of coordination polymers (CPs). The only example was associated with the Er/*R*, *S*-pempH$_2$ [*R*,

*S*-pempH$_2$ = *S*-(1-phenylethylamino)methylphosphonic acid)] system, where the addition of salt led to a change in the crystal structure from a triple-stranded helix to a quadruple-stranded helix [50]. To our knowledge, salt effect on the morphology and helical sense of chiral CPs has not been documented.

Our previous work has shown that the synergistic effect of pH and anion is crucial for the formation and helical sense of the macroscopic superhelices of the Tb(NO$_3$)$_3$/*R*, *S*-pempH$_2$ and GdX$_3$/*R*, *S*-pempH$_2$ (X = Cl$^-$, Br$^-$, I$^-$, CH$_3$SO$_3^-$, C$_6$H$_5$SO$_3^-$, CF$_3$SO$_3^-$) systems [51,52]. The pH can modulate the degree of deprotonation of the phosphonic acid moiety and, thus, the ratio of coexisting different types of chains, while the anion can modulate the interactions between chains and, thus, the formation and chiral sense of the superhelices. Considering the unique structure of the nitrate ion, a triangular-shaped singly charged oxygen anion, it not only can provide interactions through coordination bonds [53–56], but also act as a three-directional hydrogen receptor that affects the assembly of molecular building blocks [57–60]. Therefore, we hypothesize that the addition of extra nitrate salt with different concentrations into the Ln(NO$_3$)$_3$/*R*, *S*-pempH$_2$ system may tune the interchain non-covalent interactions, disturb the self-assembling environment, and provide a driving force to control the chiral sense of resulting helical products.

In this work, we chose Gd(NO$_3$)$_3$/*R*-pempH$_2$ and systematically investigated the role of pH and salt in regulating the morphology of the products (Scheme 1). We found that pure phases of blocky crystals of (H$_3$O)[Gd$_6$(*R*-pempH$_2$)$_3$(*R*-pempH)$_{15}$](NO$_3$)$_4$·9H$_2$O (***R*-Block**) were obtained at pH 2.6–2.9, and rod-like crystals of [Gd(*R*-pempH)$_3$].1.5H$_2$O (***R*-Rod**) at pH 4.2–4.6. When the pH was in between, left-handed superhelices (***R*-M**) appeared as a minor phase at pH 2.9–3.2, while right-handed superhelices (***R*-P**) were isolated as a pure phase at pH 3.6–4.2. Interestingly, the addition of 2.0 eq NaNO$_3$ salt to the reaction mixture at pH = 3.8 leads to the chirality inversion of superhelices from right-handed to left-handed. This is the first example of chirality inversion of helical structures of coordination polymers by changing the concentration of salt.

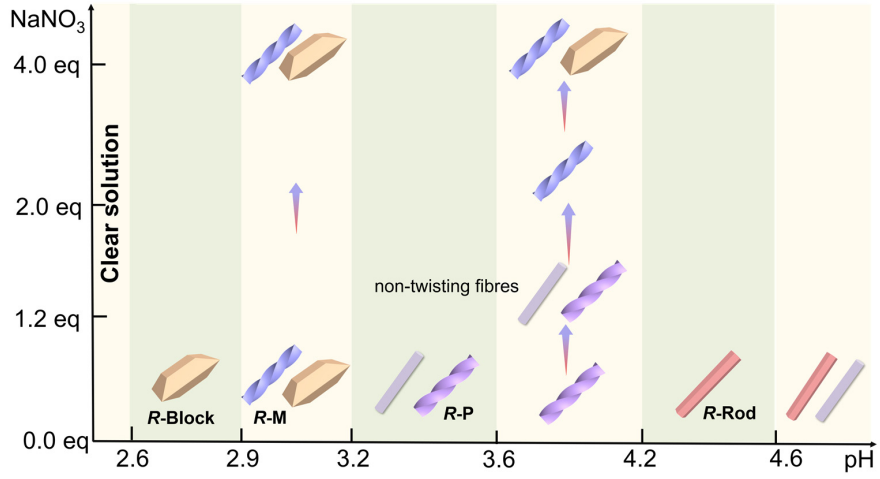


**Scheme 1.** Hydrothermal reaction products of *R*-pempH$_2$ and Gd(NO$_3$)$_3$ at different pH and salt concentrations.

## 2. Results

### *2.1. pH Effect on the Reaction Product*

The hydrothermal reaction of a mixture of Gd(NO$_3$)$_3$·6H$_2$O and *R*-pempH$_2$ (molar ratio 1:5) at 120 °C for 24 h resulted in products with differet morphologies depending on the pH of the reaction mixture (Scheme 2, Figure 1 and Figure S1). We obtained a pure phase of block-like crystals of (H$_3$O)[Gd$_6$(*R*-pempH$_2$)$_3$(*R*-pempH)$_{15}$](NO$_3$)$_4$·9H$_2$O (***R*-Block**) at pH 2.6–2.9. When the pH was 3.0–3.2, a mixture of left-handed superhelices (***R*-M**, minor phase) and block-like crystals (***R*-Block**) was observed. When the pH was raised to 3.7–4.2, a pure phase of right-handed superhelices (***R*-P**) was collected. At an even higher pH

(4.3–4.6), rod-like crystals of [Gd(*R*-pempH)$_3$]·2H$_2$O (***R*-Rod**) were isolated. It is apparent that pH plays an important role in the self-assembly process and the chirality transcription and amplification of the system. This phenomenon has been previously observed in the Tb(NO$_3$)$_3$/*R*-pempH$_2$ system [51]. However, the observation of left-handed superhelices of ***R*-M** as a minor phase at pH = 3.0–3.2 is unprecedented. To exclude the possible effect of metal ions, we conducted the same reaction but using Tb(NO$_3$)$_3$ to replace Gd(NO$_3$)$_3$. Left-handed superhelices were again obtained as a minor phase (Figure S2). Noting that the experimental condition such as the filling degree of the autoclave (ca. 53%) is not exactly the same as we used in previous work (>90%), we conducted similar hydrothermal reactions of Gd(NO$_3$)$_3$·6H$_2$O and R-pempH$_2$ but with different filling degrees (30, 50, 60, 70, 90%) at pH 3.2. As shown in Figure S3, the left-handed superhelices of ***R*-M** appeared together with ***R*-Block** when the filling degree was 30 and 50%, and vanished when the filling degree was 60%. When the filling degree was 70 and 90%, only right-handed superhelices of ***R*-P** were obtained. As the filling degree is directly related to the auto-generated pressure inside the autoclave, the above results indicate that pressure also plays an important role in the formation of the superhelices of Gd/*R*, *S*-pempH$_2$ products. When the filling degree is ca. 50%, left-handed superhelices of ***R*-M** can form, and the chirality inversion can be achieved by adjusting the pH from 3.0–3.2 to 3.7–4.2.

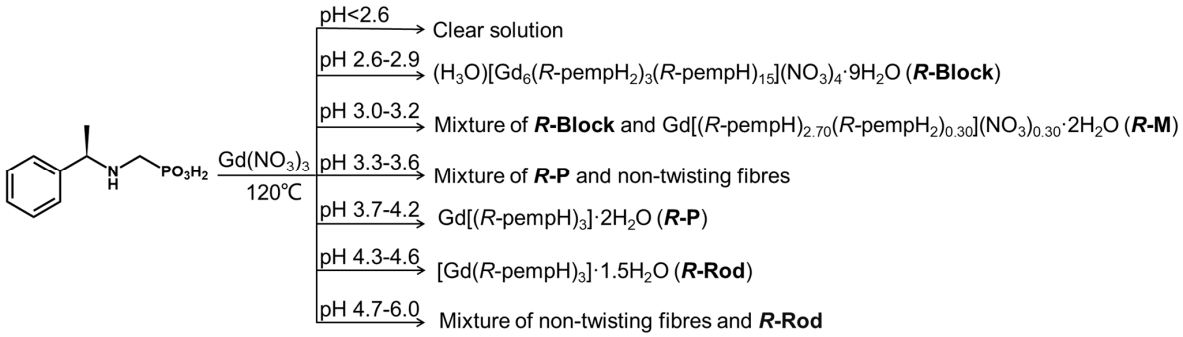


**Scheme 2.** Synthetic products of the Gd(NO$_3$)$_3$/*R*-pempH$_2$ system obtained under hydrothermal conditions (120 °C for 24 h) at different pH.

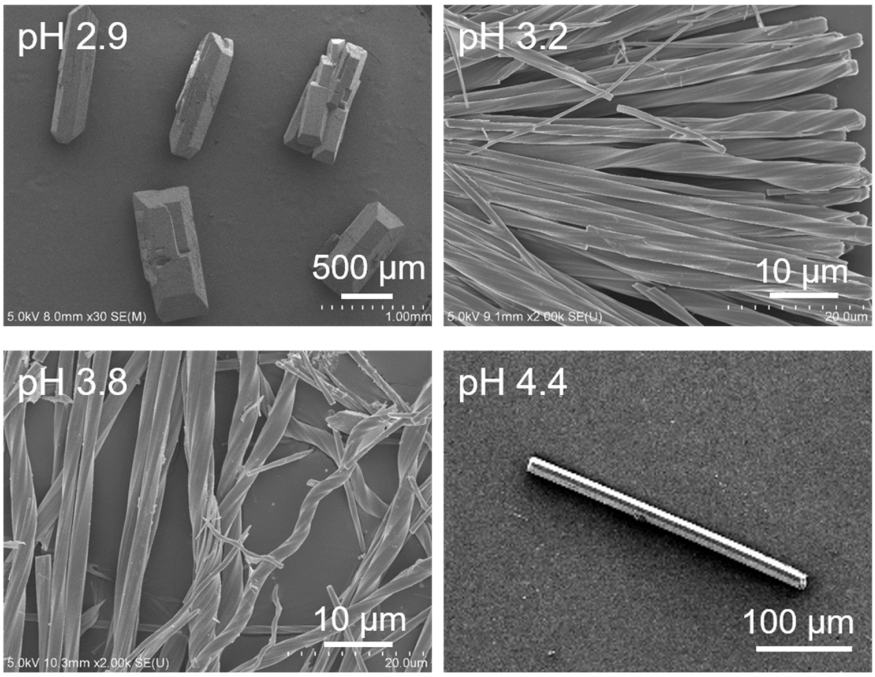


**Figure 1.** SEM images showing the morphologies of the reaction products of the Gd(NO$_3$)$_3$/*R*-pempH$_2$ system obtained under hydrothermal conditions (120 °C for 24 h) at different pH.

### 2.2. Structures of ***R*-Block** and ***R*-Rod**

Structural analyses showed that ***R*-Block** and ***R*-Rod** are isostructural to their Tb analogues [51]. ***R*-Block** crystallizes in the monoclinic system, with chiral space group $P2_1$. The asymmetric unit contains three $Gd^{3+}$, three *R*-pempH$_2$, fifteen *R*-pempH$^-$, four $NO_3^-$ anions, one $H_3O^+$ and eleven lattice water molecules (Table S1 and Figure S6). There are two kinds of positively charged chains in the structure. Chain I has the composition $[Gd_3(R\text{-pempH}_2)_2(R\text{-pempH})_7]^{2+}$, where three distinct Gd atoms, two different *R*-pempH$_2$ and seven different *R*-pempH$^-$ are found. Each Gd atom is eight-coordinated by oxygen atoms from the phosphonate groups. The Gd-O bond lengths lie in the range 2.310(5)–2.631(5) Å, and the O-Gd-O bond angles are 58.6(2)–157.4(2)° (Table S2). The amino groups in the ligands are all protonated, while the phosphonate groups in the two R-pempH$_2$ ligands are singly protonated at O18 and O27, but those in the seven *R*-pempH$^-$ ligands are fully deprotonated. The Gd atoms are triply bridged by one O-P-O and two $\mu_3$-O(P) units, forming an infinite triple-stranded chain running along the b-axis (Figure 2). The pitch and diameter are 24.21 and 18.88 Å, respectively, for Chain I (Figure 2). The protonated phosphonate oxygen atoms O18 and O27 are involved in hydrogen bonding with the counteranion $NO_3^-$ [O27 . . . O63: 2.545(8) Å, O18 . . . O55: 2.462(19) Å] (Figure 3a).

Chain II has the composition $[Gd_3(R\text{-pempH}_2)(R\text{-pempH})_7]^+$ which contains one less *R*-pempH$_2$ than Chain I. In addition, one of the three Gd atoms (Gd4) in Chain II is seven-coordinated and the other two (Gd5, Gd6) are eight-coordinated, unlike Chain I in which all Gd atoms are eight-coordinated. As a result, the Gd atoms in Chain II are bridged by one O-P-O and two $\mu_3$-O(P) units forming a trimer, and then the trimers are further linked by two O-P-O and one $\mu_3$-O(P) units forming a triple-stranded infinite chain (Figure 2). Again, the phosphonate group in *R*-pempH$_2$ is singly protonated at O30 and is involved in hydrogen bonding with the nitrate anion. Compared to Chain I, the pitch of Chain II (24.21 Å) is the same, but the diameter (17.91 Å) is smaller (Figure 2).

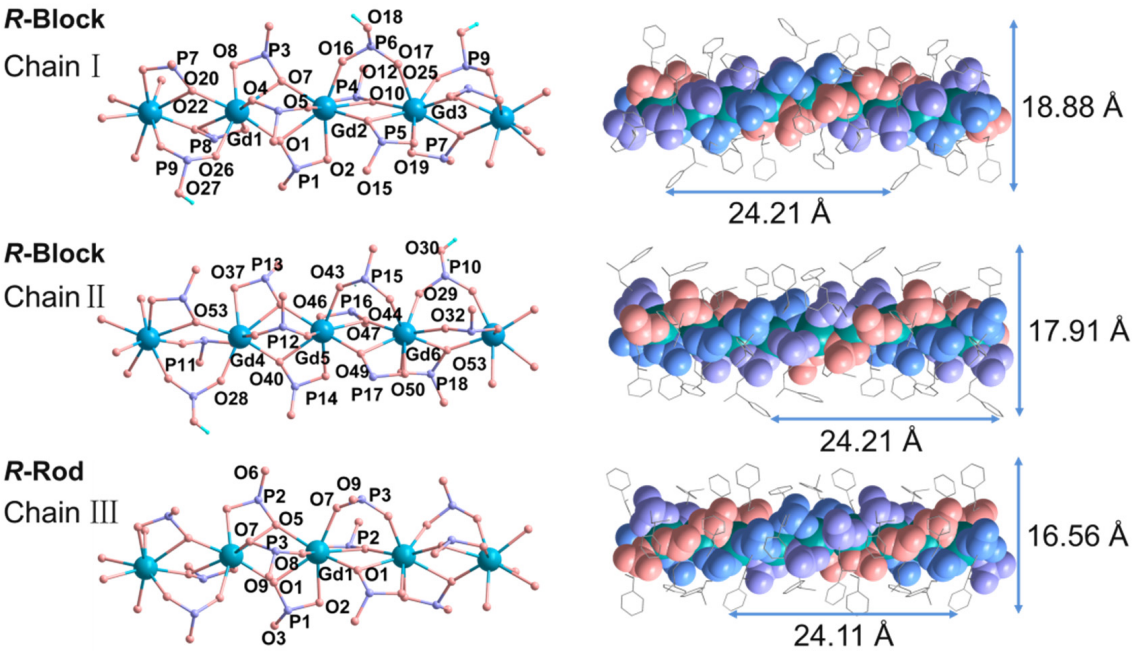


**Figure 2.** A fragment of the chain structure in ***R*-Block** and ***R*-Rod**. Left: Ball and stick representation with atomic labelling. All C and N atoms are omitted for clarity. Right: Space filling representation showing left-handed triple strands in the structure. The pitch and diameter of each helical chain are also given. The structure of ***R*-Rod** is adapted from ref. [52].

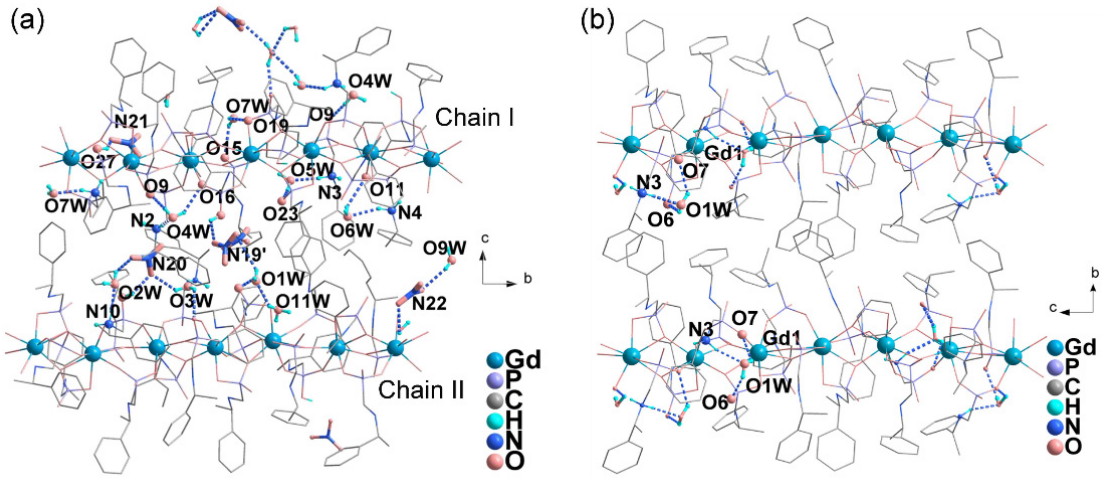


**Figure 3.** Packing diagrams of structures of ***R*-Block** (**a**) and ***R*-Rod** (**b**). The dotted lines represent the hydrogen bonding interactions. The structure of ***R*-Rod** is adapted from ref. [52].

The positively charged Chains I and II are stacked in the lattice. Between the chains, there are four crystallographically different $NO_3^-$ anions and one $H_3O^+$ to balance the charge, as well as lattice water molecules. Therefore, an extensive hydrogen bonding network is found among the phosphonate oxygen atoms, the amino groups, the $NO_3^-$ anions, and the water molecules (Figure 3a). The shortest interchain distance is 15.334 Å (Figure S7).

The structure of compound ***R*-Rod** was previously reported [52]. It crystallizes in the hexagonal systems, chiral group $P6_5$, and has a general formula of $[Gd(R\text{-pempH})_3]\cdot 1.5H_2O$. Only one distinct Gd atom is observed in the structure, which is eight-coordinated by oxygen atoms from six *R*-pempH$^-$ (Figure 2). The Gd-O bond lengths lie in the range 2.285(13)–2.606(14) Å, and the O-Gd-O bond angles are 58.7(4)–161.1(4)°. ***R*-Rod** shows a neutral chain structure, where the Gd atoms are triply bridged by one O-P-O and two $\mu_3$-O(P) units. Compared to ***R*-Block**, although the pitch of the resulting triple-stranded chain (Chain III) in ***R*-Rod** is similar (24.11 Å vs. 24.21 Å in Chain I and II), the chain diameter is much shorter (16.56 Å vs. 18.88 Å in Chain I and 17.91 Å in Chain II) (Figure 2). The inter-chain distance is 15.756 Å. The lattice water molecules are located close to the chains and form hydrogen bonds with the phosphonate oxygen and amino nitrogen atoms [O1W . . . O6: 2.770(4) Å, O1W . . . O7: 2.970(3) Å, N3 . . . O1W: 2.880(3) Å]. The interchain interactions are dominated by van der Waals contacts (Figure 3b).

### *2.3. Characterization of Superhelices* ***R*-M** *and* ***R*-P**

Since superhelix ***R*-M** was obtained as a minor phase together with block-like crystals, we collected the sample by manual separation, while ***R*-P** was obtained as a pure phase at pH 3.8. To determine the composition of ***R*-M** and ***R*-P**, we performed energy dispersive X-ray spectroscopy (EDS), thermogravemetic (TG) ananlysis and elemental analysis. The EDS measurements revealed a molar ratio of Gd:P = 1:3 in both cases (Figure S8). By combining with the TG and elemental analysis results (Figure S9, Table S3), we propose that the molecular formulae of ***R*-M** and ***R*-P** are $Gd[(R\text{-pempH})_{2.70}(R\text{-pempH}_2)_{0.30}](NO_3)_{0.30}\cdot 2H_2O$ and $Gd[(R\text{-pempH})_3]\cdot 2H_2O$, respectively.

Noting that the chemical composition of ***R*-P** is similar to that of ***R*-Rod** and that both products are obtained at very similar pH conditions, we envisage that the structure of ***R*-P** is closely related to that of ***R*-Rod**. Indeed, the PXRD patterns of both are very similar except that the peaks on the ***R*-P** pattern are all shifted to the left (Figure 4a). The result suggests that ***R*-P** has a similar structure to ***R*-Rod**, but with an enlarged unit cell volume. This is reasonable because the chain stacking in the superhelix ***R*-P** may be looser than that in the crystal ***R*-Rod**. To obtain the cell parameters of ***R*-P**, we indexed the diffraction peaks of ***R*-P** and ***R*-Rod** using TOPAS 5.0 [61], yielding the parameters: space group $P6_5$,

a = 16.34 Å, c = 24.40 Å, V = 5641.98 Å$^3$ for ***R*-P**; and $P6_5$, 15.86 Å, c = 24.23 Å, V = 5298.37 Å$^3$ for ***R*-Rod** (Figure S10). Compared to ***R*-Rod**, the cell volume of ***R*-P** is expanded by ca. 343 Å$^3$ (5641.98 Å$^3$ vs. 5298.37 Å$^3$ in ***R*-Rod**).

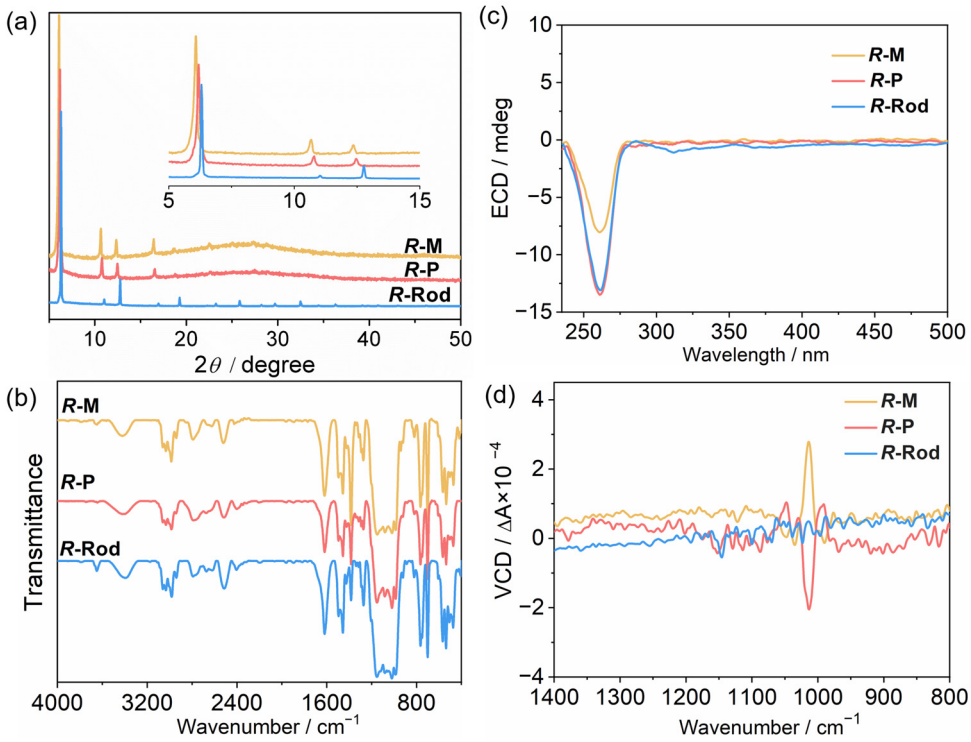


**Figure 4.** (**a**) PXRD patterns; (**b**) CD spectra; (**c**) IR spectra; (**d**) VCD spectra of **R-M**, ***R*-P** and ***R*-Rod**.

Although the PXRD patterns of ***R*-P** and ***R*-Rod** are slightly different, their infred (IR) spectra are identical (Figure 4b). Both show a series of peaks between 900 and 1200 cm$^{-1}$, assigned to the ν(P-O) stretching vibrations. The solid-state circular dichroism (CD) spectra are also identical, and both exhibit a negative Cotton effect at 262 nm (Figure 4c), attributed to the π-π* transitions of the chiral phosphonate ligand [62]. These results corroborate the structural similarity and chiral nature of ***R*-P** and ***R*-Rod** at the molecular level. Strong evidence to distinguish the difference between ***R*-P** and ***R*-Rod** is their vibrational circular dichroism (VCD) spectra. As shown in Figure 4d, ***R*-P** exhibits a strong negative VCD signal at 1014 cm$^{-1}$ and three weak positive VCD signals near 1048, 1030, and 990 cm$^{-1}$. In contrast, the peak at 1014 cm$^{-1}$ is absent in the VCD spectrum of ***R*-Rod**. Clearly, the helical morphology of ***R*-P** is reflected by its VCD spectrum.

Unlike ***R*-P**, the left-handed superhelix ***R*-M** was obtained at a lower pH and its formula contains 0.3 $NO_3^-$ anions per Gd. The IR spectrum of ***R*-M** is similar to that of ***R*-P** except for the enhanced intensity of the peak at 1385 cm$^{-1}$, attributed to the stretching vibration of the un-coordinated $NO_3^-$ (Figure 4b). The results suggest that the phosphonate groups in ***R*-M** are partially protonated, forming positively charged chains which are balanced by nitrate anions. The intercalation of nitrate anions may increase the interchain distance and expand the cell volume. This is confirmed by the PXRD measurements. Compared to ***R*-P**, ***R*-M** shows an identical PXRD pattern, but the diffraction peaks are all left-shifted (Figure 4a). A Pawley fit of the PXRD pattern of ***R*-M** using TOPAS 5.0 led to the unit cell parameters: space group $P6_5$, a = 16.73 Å, c = 40.30 Å, V = 9767.22 Å$^3$ (Figure S10). The c-axis is significantly enlongated, which can be explained by the possible symmetry reduction of the chain structure due to the incorporation of nitrate anions. The CD spectrum of ***R*-M** is similar to that of ***R*-P** (Figure 4c), in agreement with the existence of the same chiral ligand in the two materials. Interestingly, the VCD profile of ***R*-M** is almost a mirror of that of ***R*-P**, where a positive signal was found near 1014 cm$^{-1}$ and three weak

negative signals near 1048, 1030 and 990 $cm^{-1}$ (Figure 4d). This result is consistent with their macroscopic helix structure, i.e., the ***R*-P** superhelix is right-handed, while the ***R*-M** superhelix is left-handed.

The formation of the ***R*-M** and ***R*-P** superhelices with similar chemical composition and structure but opposite handedness demonstrates that helical inversion may be achieved for the $Gd(NO_3)_3$/*R*-pempH$_2$ system by adjusting the pH of the reaction mixture. When the pH is low, the phosphonate groups are partially protonated resulting in positively charged chains. The incorporation of a suitable amount of nitrate anions may affect the chain packing in the lattice and, thus, the formation of left-handed superhelix ***R*-M**. A slight increase in the pH leads to the deprotonation of the phosphonate groups and the decrease in the amount of nitrate anions. As a result, right-handed superhelix ***R*-P** is obtained in order to maximize the van der Waals contacts. The same phenomenon was previously observed for the $GdX_3$/*R*-pempH$_2$ (X = I, $CF_3SO_3^-$) system [52]. Noting that ***R*-M** appeared as a minor phase at pH 3.2, we envisage whether it is possible to isolate a pure phase of ***R*-M** and accomplish chirality inversion through a combined effect of pH and salt.

### *2.4. Salt Effect on the Chirality Inversion of Superhelices*

We first investigated the effect of additional $NaNO_3$ on the product of the $Gd(NO_3)_3$/*R*-pempH$_2$ reaction mixture. The above-mentioned results have shown that a pure phase of right-handed superhelix ***R*-P** can be obtained at pH 3.8 without the addition of extra $NaNO_3$. By keeping the initial pH at 3.8, we conducted similar hydrothermal reactions of $Gd(NO_3)_3$/*R*-pempH$_2$ at 120 °C for 24 h, but with the addition of different amounts of $NaNO_3$. As shown in Figure 5 and Figure S11, right-handed superhelices dominated when the added $NaNO_3$ was below 0.8 eq (vs. $Gd(NO_3)_3$). When the amount of $NaNO_3$ was 1.2 eq, left-handed superhelices emerged together with nanofibers without clear helicity. When the amount of $NaNO_3$ was further increased to 2.0–3.0 eq, a pure phase of left-handed superhelix (named as ***R*-M'**) was collected. When the amount of $NaNO_3$ was above 4.0 eq, block-like crystals ***R*-Block** were obtained together with ***R*-M'**. It is clear that chirality inversion of the $Gd(NO_3)_3$/*R*-pempH$_2$ system can be achieved by controlling the amount of extra $NaNO_3$ salt at pH 3.8.

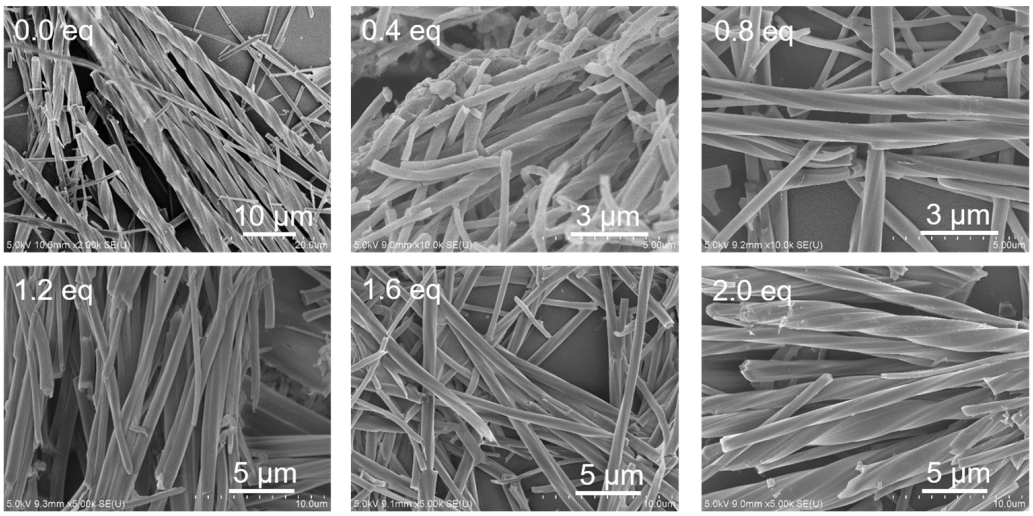


**Figure 5.** SEM images of the products after hydrothermal reactions of $Gd(NO_3)_3$ and *R*-pempH$_2$ with different amounts of $NaNO_3$ at 120 °C and pH 3.8 for 24 h.

Except for the morphology change, the salt-induced chirality inversion from ***R*-P** to ***R*-M'** was accompanied by other changes. The C:N molar ratio decreased from 8.9:1 to 7.8:1 when adding 0.0–2.0 eq $NaNO_3$ (Table S1), suggesting the incorporation of nitrate anions. This is confirmed by the IR spectra which show an increase in peak intensity at 1385 $cm^{-1}$ (Figure S12). The PXRD patterns showed a slight left-shift of the peaks

(Figure S13). Although the CD spectra remained similar (Figure S14), a significant change was observed in the VCD spectra (Figure S15). With 0.0 eq $NaNO_3$, we obtained ***R*-P** which exhibits a strong negative VCD signal at ca. 1014 $cm^{-1}$. This peak intensity was reduced for the product with 0.4 eq $NaNO_3$. Interestingly, the sign of this signal became opposite with 0.8 eq $NaNO_3$, and the intensity increased for the products with increasing amount of $NaNO_3$.

To examine whether ***R*-M'** is the same as ***R*-M**, we characterized the products by different techniques. Both the IR spectrum and PXRD pattern of ***R*-M'** are identical to those of ***R*-M** (Figures S16 and S17). The Pawley fit of the PXRD pattern of ***R*-M'** led to similar unit cell parameters: space group $P6_5$, a = 16.82 Å, c = 40.37 Å, V = 9890.22 $Å^3$ (Figure S18). The elemental and thermal analysis confirmed that **R-M'** has a chemical composition of $Gd[(R\text{-pempH})_{2.70}(R\text{-pempH}_2)_{0.30}](NO_3)_{0.30}\cdot 2H_2O$ (Figure S19 and Table S3), in agreement with that for ***R*-M**. In addition, both CD and VCD profiles of ***R*-M'** coincide with those of ***R*-M** (Figures S20 and S21). Based on these results, we conclude that ***R*-M'** is the same as ***R*-M**, both in composition and chiral structure.

We next questioned whether the cation or the anion in the added $NaNO_3$ salt plays a key role in the chirality inversion of the $Gd(NO_3)_3/R\text{-pempH}_2$ reaction product. We conducted the same reactions at pH 3.8, but with adding different salts of $Ba(NO_3)_2$, $KNO_3$ and $NaNO_3$ (2.0 eq $NO_3^-$). In all cases, we obtained the same product ***R*-M** (Figures S22–S25), indicating that the cation of salt does not affect the final product. We then conducted the same reactions at pH 3.8, but with the addition of 2.0 eq salts of NaCl, NaBr, $NaNO_2$, and $Na_2SO_4$. We obtained a mixture of right-handed superhelix ***R*-P** and non-twisted fibers for NaCl and NaBr. For $NaNO_2$ and $Na_2SO_4$, we obtained unrecognized new phases with of nanoplate and nanoparticle morphologies, respectively (Figures S26–S28). The results corroborate that it is the nitrate anion of the salt that plays a vital role in directing the chirality inversion from ***R*-P** to ***R*-M**.

To further evaluate the influence of pH on the reaction product, we performed the same reactions containing an additional 2.0 eq $NaNO_3$, except for the pH value. As revealed by the SEM images, left-handed superhelices ***R*-M** can be obtained at pH 3.0–3.8 (Figure S29). At pH 4.0, non-helical fibers were dominant. When the pH was further increased to 4.4, pure right-handed superhelices ***R*-M** were obtained. Clearly, with additional salt of $NaNO_3$ in the reaction mixture, the pH value to obtain ***R*-P** is much higher. Therefore, the chiral sense of superhelices can be controlled by both pH and nitrate salt.

To understand the mechanism of salt-induced chirality inversion, we monitored the hydrothermal reaction products of mixtures containing 2.0 eq $NaNO_3$ at pH 3.8 and 120 °C for different periods of time. When the reaction time was less than 30 min, only nanoparticles appeared on the surface of $R\text{-pempH}_2$ ligand (Figure S30). The nanoparticles grew with increasing reaction time. At 3 h, nanorods with a diameter of ca. 150 nm and a length of ca. 500 nm were observed, which have a P/Gd ratio of ca. 2.9/1, very close to that for ***R*-M** (Figure S31). After 4 h of reaction, we obtained a pure phase of left-handed superhelix **R-M**, confirmed by the SEM, EDS, IR, and PXRD measurements (Figures S30–S33). The average width of ***R*-M** increased with prolonging the time, from ca. 0.5 μm at 4 h to 2 μm at 12 h. The results indicate that the left-handed superhelix ***R*-M** is formed from the very beginning. This means that the nitrate salt is involved in the self-assembly process at the nucleation stage. In general, the role of the nitrate anion can be three-fold. The first is its coordination capability towards metal ions. The second is its ability to form an extensive hydrogen bonding network with phosphonate ligands and water molecules. The third is its ability to adjust the ionic strength of the reaction mixture. Since the nitrate anion is uncoordinated in the present cases, the latter two factors should be more important. The existence of extra nitrate anions may facilitate the H-bonding interaction between the nitrate anions and chains, which, in turn, stabilizes the positively charged chains at relatively high pH in order to keep the overall charge balanced. The tendency to maintain $NO_3^-$ anions in the lattice and meanwhile release protons from phosphonate groups at pH 3.8 may cause a mismatch between the chains, leading to the twisted growth of the chains and the formation of ***R*-M** [63]. However, we noticed that

***R*-M** appeared as a minor phase when 1.2 eq $NaNO_3$ was added, and as a pure phase when 2.0–3.0 eq $NaNO_3$ was added. The concentration of salt is related to the ionic strength of the reaction mixture according to the equation: $I = 1/2\sum c_i z_i^2$, where $I$ is the ionic strength, $c_i$ is the concentration of various ions, and $z_i$ is the number of the charges carried by each ion. Increasing the ionic strength will increase the Debye−Hückel shielding, reduce the electronic attraction between $Gd^{3+}$ and $pempH^-$, and improve contact opportunities between $Gd^{3+}$ and nitrate anion. Therefore, it is the combined effect of the hydrogen bonding ability of the nitrate anion and the ionic strength that is responsible to the salt-induced chirality inversion of the macroscopic superhelices of the present Gd coordination polymers (Scheme 3).

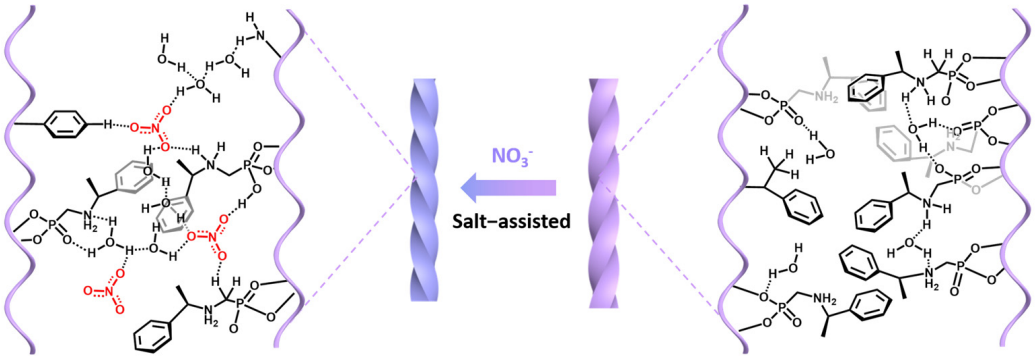


**Scheme 3.** Salt-assisted macroscopic chirality inversion of Gd coordination polymers.

## 3. Conclusions

In summary, we systematically investigated the role of pH and salt in regulating the morphology of the products in a $Gd(NO_3)_3$/*R*-$pempH_2$ system. The products of ***R*-Block, *R*-M, *R*-P** and ***R*-Rod** were obtained via pH and salt modulation. This is because pH determines the deprotonation degree of the ligand, and $NO_3^-$ modulates the interchain interaction. Without extra $NO_3^-$, chirality inversion from the left-handed superhelix ***R*-M** to the right-handed superhelix ***R*-P** can be achieved by pH modulation from 3.2 to 3.8. However, ***R*-M** was obtained only as a minor phase. The addition of $NaNO_3$ (2.0 eq) at pH 3.8 results in an inversion of chiral sense from ***R*-P** to ***R*-M** as a pure phase. The important role nitrate salt plays in the helicity inversion of the present system may originate from the strong ability of the nitrate anion as a hydrogen bonding receptor and the increased ionic strength of the reaction mixture which improved the nitrate-chain interactions. To our knowledge, this is the first example of salt-assisted macroscopic helical inversion in artificial systems. This work provides a new strategy for the design and synthesis of functional coordination polymers with desired macroscopic helicity.

## 4. Materials and Methods

### *4.1. Materials and Physical Measurements*

R−(1−phenylethylamino)methylphosphonic acid (*R*-$pempH_2$) was synthesized according to procedures given in the previous literature [64]. All reagents were purchased from commerical sources without further purification. The morphologies of suprehelices were characterized on a scanning electron microscope (SHIMADZU, SSX-550, Kyoto, Japan) at an acceleration voltage of 5 kV. The UV–Vis spectra of products were recorded on a Perkin Elmer Lambda 950 UV/VIS/NIR spectrometer (Perkin Elmer, Waltham, MA, USA) using powder samples. Elemental analyses were carried out on a PE 240C analyzer (Perkin Elmer, America). Powder X-ray diffraction (PXRD) data were obatined on a Bruker D8 advance diffractometer with Cu-$K_\alpha$ radiation. Fourier infrared spectra were recorded on a Bruker Tensor 27 spectrometer (Bruker, Leipzig, Germany) with pressed KBr pellets in the range 4000–400 $cm^{-1}$. Thermogravimetric (TG) analyses were measured on a Mettler Toledo TGA/DSC instrument(Mettler 5MP/PF7548/MET/400W, Mettler-Toledo, Greifensee, Switzerland) in the range of 30–600 °C under a nitrogen flow (20 mL/min) at

a heating rate of 5 °C $min^{-1}$. CD spectra of products were recorded on a circular dichroism spectrophotometer (JASCO, J-810, Tokyo, Japan) at room temperature. VCD spectra were recorded on a Bruker VERTEX 80v Fourier transform infrared spectrometer (Bruker, Germany) equipped with a PMA 50 VCD/IRRAS module (Bruker, Germany).

### *4.2. Synthesis of $(H_3O)[Gd_6(R\text{-}pempH_2)_3(R\text{-}pempH)_{15}]\ (NO_3)_4{\cdot}9H_2O$ (**R-Block**)*

A mixture of *R*-pempH$_2$ (0.1080 g, 0.5 mmol) and Gd(NO$_3$)$_3$·6H$_2$O (0.0451 g, 0.1 mmol) was stirred for half an hour in 6 mL H$_2$O. Later, the pH was adjusted to 2.9 with 0.5 mol/L NaOH. The glass bottle was then kept in a 15 mL Teflon-lined autoclave, adding 2.0 mL deionized water in the outside of the glass bottle, and heated at 120 °C for 24 h. After cooling to the room temperature, block-shaped colorless crystals of ***R*-Block** were obtained, which were washed with deionized water several times and collected. Yield: 17.3% (15.1 mg) based on Gd(NO$_3$)$_3$. Elemental analysis (%) calculated for $C_{162}H_{238}N_{22}O_{66}P_{18}Gd_6{\cdot}10H_2O$: C, 37.21; H, 4.94; N, 5.89. Found: C, 37.09; H, 4.98; N, 5.90. IR (KBr, $cm^{-1}$): 3446 (w), 3066 (m), 3023 (m), 2986 (m), 2790 (m), 2523 (w), 2405 (m), 1622 (m), 1497 (m), 1456 (m), 1431 (m), 1384 (m), 1313 (m), 1292 (m), 1158 (s), 1083 (s), 1010 (s), 986 (s), 819 (w), 766 (m), 751 (m), 702 (m), 565 (m), 536 (m), 506 (m), 473 (m). Thermal analysis confirmed the removal of ten water molecules below 100 °C (obs. 3.6%, calcd. 3.4%). The number of water molecules is less than that determined by single crystal structural analysis, possibly due to the loss of two lattice water molecules in air.

### *4.3. Synthesis of $Gd[(R\text{-}pempH)_{2.70}(R\text{-}pempH_2)_{0.30}](NO_3)_{0.30}{\cdot}2H_2O$ (**R-M**)*

***R*-M** was obtained following a similar procedure except that pH was adjusted to 3.2. A white powder of ***R*-M** was obtained, which was washed with deionized water several times and collected. Yield: 3.0% (2.5 mg) based on Gd(NO$_3$)$_3$. Elemental analysis (%) calculated for $C_{29}H_{39.3}N_3O_9P_3Gd{\cdot}0.30NO_3{\cdot}2H_2O$: C, 37.92; H, 5.07; N, 5.42. Found: C, 37.93; H, 5.03; N, 5.58. IR (KBr, $cm^{-1}$): 3426 (w), 3065 (m), 3036 (m), 2987 (m), 2794 (m), 2522 (w), 1623 (m), 1493 (m), 1456 (m), 1384 (m), 1314 (w), 1292 (w), 1273 (w), 1151 (s), 1079 (s), 1017 (s), 985 (s), 939 (m), 822 (w), 765 (m), 751 (m), 702 (m), 565 (m), 536 (m), 504 (m), 472 (m). Thermal analysis confirmed the removal of two water molecules below 120 °C (obs. 3.9%, calcd. 4.2%).

### *4.4. Synthesis of $Gd[(R\text{-}pempH)_3]{\cdot}2H_2O$ (**R-P**)*

***R*-P** was obtained following a similar procedure except that pH was adjusted to 3.8. A white powder of ***R*-P** was obtained, which was washed with deionized water several times and collected. Yield: 18.8% (15.7 mg) based on Gd(NO$_3$)$_3$. Elemental analysis (%) calculated for $C_{27}H_{39}N_3O_9P_3Gd{\cdot}2H_2O$: C, 38.80; H, 5.15; N, 5.03. Found: C, 38.78; H, 5.03; N, 5.05. IR (KBr, $cm^{-1}$): 3430 (w), 3060 (m), 3032 (m), 2984 (m), 2787 (w), 2526 (w), 1627 (m), 1497 (m), 1482 (m), 1456 (m), 1384 (m), 1314 (w), 1290 (w), 1277 (w), 1151 (s), 1082 (s), 1018 (s), 986 (s), 941 (m), 818 (w), 763 (m), 752 (m), 701 (m), 564 (m), 535 (m), 503 (m), 470 (m). Thermal analysis confirmed the removal of two water molecules below 120 °C (obs. 4.6%, calcd. 4.3%).

### *4.5. Synthesis of $Gd[(R\text{-}pempH)_{2.70}(R\text{-}pempH_2)_{0.30}](NO_3)_{0.30}{\cdot}2H_2O$ (**R-M'**)*

***R*-M'** was obtained following a similar procedure to ***R*-P** except that 2.0 eq NaNO$_3$ was added to the reaction mixture. White powder of ***R*-M'** was obtained, washing with deionized water for several times and collecting. Yield: 16.7% (14.3 mg) based on Gd(NO$_3$)$_3$. Elemental analysis (%) calculated for $C_{29}H_{39.3}N_3O_9P_3Gd{\cdot}0.30NO_3{\cdot}2H_2O$: C, 37.94; H, 5.07; N, 5.41. Found: C, 37.94; H, 4.89; N, 5.66. IR (KBr, cm-1): 3422 (w), 362 (m), 3036 (m), 2983 (m), 2794 (m), 2515 (w), 1623 (m), 1496 (m), 1455 (m), 1384 (m), 1315 (w), 1292 (w), 1274 (w), 1152 (s), 1083 (s), 1019 (s), 985 (s), 923 (w), 822 (w), 765 (m), 751 (m), 699 (m), 566 (m), 536 (m), 505 (m), 473 (m). Thermal analysis confirmed the removal of two water molecules below 120 °C (obs. 4.3%, calcd. 4.2%).

### *4.6. Single Cryatal X-ray Crystallography*

Single crystal data of ***R*-Block** were collected on a Bruker APEX DUO (for R-Block) diffractometer using graphite-monochromated Mo Kα radiation, λ = 0.71073 Å. The data were integrated using the Siemens SAINT program [65]. Adsorption corrections were applied. The structure was solved by direct methods and refined on $F^2$ by full-matrix least-squares using SHELXTL [66]. All non-hydrogen atoms were refined anisotropically. All hydrogen atoms bound to carbon were refined isotropically in riding mode. For ***R*-Block**, hydrogen atoms of water molecules were detected via experimental electron density and then refined isotropically with a reasonable restriction of O-H bond distances and H-O-H angles. The residual electron densities were of no chemical significance. The crystallographic data are shown in Supplementary Table S1, and the selected bond lengths and angles are shown in Supplementary Table S2. Deposition Number 2086976 contains the supplementary crystallographic data. These data can be obtained free of charge from the Cambridge Crystallographic Data Centre via www.ccdc.cam.ac.uk/data_request/cif (accessed on 3 June 2021).

**Supplementary Materials:** The following supporting information can be downloaded at: https://www.mdpi.com/article/10.3390/molecules28010163/s1, Figures S1–S33 and Tables S1–S3 see Supporting Information.

**Author Contributions:** Conceptualization, L.-M.Z., T.H. and L.-Q.W.; methodology, T.H., L.-Q.W. and Y.X.; formal analysis, T.H., S.-S.B. and L.-M.Z.; investigation, T.H., L.-Q.W. and Y.X.; data curation, T.H. and S.-S.B.; writing—original draft preparation, T.H.; writing—review and editing, L.-M.Z.; supervision, L.-M.Z.; project administration, L.-M.Z.; funding acquisition, L.-M.Z. All authors have read and agreed to the published version of the manuscript.

**Funding:** This research was funded by the National Natural Science Foundation of China (21731003, 91956102).

**Institutional Review Board Statement:** Not applicable.

**Informed Consent Statement:** Not applicable.

**Data Availability Statement:** Data are available from the authors.

**Conflicts of Interest:** The authors declare no conflict of interest.

## References

1. Das, R.K.; Zouani, O.F.; Labrugere, C.; Oda, R.; Durrieu, M.C. Influence of Nanohelical Shape and Periodicity on Stem Cell Fate. *ACS Nano* **2013**, *7*, 3351–3361. [CrossRef] [PubMed]
2. Jiang, J.; Meng, Y.; Zhang, L.; Liu, M. Self-Assembled Single-Walled Metal-Helical Nanotube (M-HN): Creation of Efficient Supramolecular Catalysts for Asymmetric Reaction. *J. Am. Chem. Soc.* **2016**, *138*, 15629–15635. [CrossRef] [PubMed]
3. Liu, M.; Zhang, L.; Wang, T. Supramolecular Chirality in Self-Assembled Systems. *Chem. Rev.* **2015**, *115*, 7304–7397. [CrossRef] [PubMed]
4. Yang, D.; Duan, P.; Zhang, L.; Liu, M. Chirality and Energy Transfer Amplified Circularly Polarized Luminescence in Composite Nanohelix. *Nat. Commun.* **2017**, *8*, 15727. [CrossRef] [PubMed]
5. Yuan, T.; Sun, Z.; Mu, A.U.; Zeng, M.; Kalin, A.J.; Cheng, Z.; Olson, M.A.; Fang, L. Assembly and Chiral Memory Effects of Dynamic Macroscopic Supramolecular Helices. *Chem. Eur. J.* **2018**, *24*, 16553–16557. [CrossRef]
6. Jiang, H.; Zhang, L.; Liu, M. Self-Assembly of 1D Helical Nanostructures into Higher Order Chiral Nanostructures in Supramolecular Systems. *ChemNanoMat* **2018**, *4*, 720–729. [CrossRef]
7. Janssen, P.G.; Ruiz-Carretero, A.; Gonzalez-Rodriguez, D.; Meijer, E.W.; Schenning, A.P. pH-Switchable Helicity of DNA-Templated Assemblies. *Angew. Chem. Int. Ed.* **2009**, *48*, 8103–8106. [CrossRef]
8. Jiang, P.; Liu, W.; Li, Y.; Li, B.Z.; Yang, Y.-G. pH-Influenced Handedness Inversion of Circularly Polarized Luminescence. *New J. Chem.* **2021**, *45*, 21941–21946. [CrossRef]
9. Kousar, A.; Liu, J.; Mehwish, N.; Wang, F.; Dang-i, A.Y.; Feng, C. pH-Regulated Supramolecular Chirality of Phenylalanine-Based Hydrogels. *Mater. Today Chem.* **2019**, *11*, 217–224. [CrossRef]
10. Kurouski, D.; Lu, X.; Popova, L.; Wan, W.; Shanmugasundaram, M.; Stubbs, G.; Dukor, R.K.; Lednev, I.K.; Nafie, L.A. Is Supramolecular Filament Chirality the Underlying Cause of Major Morphology Differences in Amyloid Fibrils? *J. Am. Chem. Soc.* **2014**, *136*, 2302–2312. [CrossRef]

11. Mason, M.L.; Lalisse, R.F.; Finnegan, T.J.; Hadad, C.M.; Modarelli, D.A.; Parquette, J.R. pH-Controlled Chiral Packing and Self-Assembly of a Coumarin Tetrapeptide. *Langmuir* **2019**, *35*, 12460–12468. [CrossRef] [PubMed]
12. Xie, Y.; Wang, Y.; Qi, W.; Huang, R.; Su, R.; He, Z. Reconfigurable Chiral Self-Assembly of Peptides through Control of Terminal Charges. *Small* **2017**, *13*, 1700999. [CrossRef] [PubMed]
13. Freire, F.; Seco, J.M.; Quinoa, E.; Riguera, R. Chiral Amplification and Helical-Sense Tuning by Mono- and Divalent Metals on Dynamic Helical Polymers. *Angew. Chem. Int. Ed.* **2011**, *50*, 11692–11696. [CrossRef] [PubMed]
14. Liu, G.; Sheng, J.; Teo, W.-L.; Yang, G.; Wu, H.; Li, Y.; Zhao, Y. Control on Dimensions and Supramolecular Chirality of Self-Assemblies through Light and Metal Ions. *J. Am. Chem. Soc.* **2018**, *140*, 16275–16283. [CrossRef]
15. Qin, P.; Wu, Z.; Li, P.; Niu, D.; Liu, M.; Yin, M. Triple-Modulated Chiral Inversion of Co-Assembly System Based on Alanine Amphiphile and Cyanostilbene Derivative. *ACS Appl. Mater. Interfaces* **2021**, *13*, 18047–18055. [CrossRef]
16. Wang, F.; Feng, C.-L. Metal-Ion-Mediated Supramolecular Chiralityof l-Phenylalanine Based Hydrogels. *Angew. Chem. Int. Ed.* **2018**, *57*, 5655–5659. [CrossRef] [PubMed]
17. Wang, F.; Ji, W.; Yang, P.; Feng, C.-L. Inversion of Circularly Polarized Luminescence of Nanofibrous Hydrogels through Co-assembly with Achiral Coumarin Derivatives. *ACS Nano* **2019**, *13*, 7281–7290. [CrossRef]
18. Zha, X.; Chen, Y.; Fan, H.; Yang, Y.; Xiong, Y.; Xu, G.; Yan, K.; Wang, Y.; Xie, Y.; Wang, D. Handedness Inversion of Chiral 3-Aminophenol Formaldehyde Resin NanotubesMediatedbyMetal Coordination. *Angew. Chem. Int. Ed.* **2021**, *60*, 7759–7769. [CrossRef]
19. Gillissen, M.A.; Koenigs, M.M.; Spiering, J.J.; Vekemans, J.A.; Palmans, A.R.; Voets, I.K.; Meijer, E.W. Triple Helix Formation in Amphiphilic Discotics: Demystifying Solvent Effects in Supramolecular Self-Assembly. *J. Am. Chem. Soc.* **2014**, *136*, 336–343. [CrossRef]
20. Mao, Y.; Liu, K.; Meng, L.; Chen, L.; Chen, L.; Yi, T. Solvent Induced Helical Aggregation in the Self-Assembly of Cholesterol Tailed Platinum Complexes. *Soft Matter* **2014**, *10*, 7615–7622. [CrossRef]
21. Urushima, A.; Ousaka, N.; Yashima, E. Tug-of-War in a Dynamic Helical Peptide: Solvent-Induced Helix-Helix Transition of a Lactam-Bridged Peptide Composed of Point- and Axial Chiralities Remote from Each Other. *Chem. Asian J.* **2018**, *13*, 3150–3154. [CrossRef] [PubMed]
22. Wang, Y.; Qi, W.; Huang, R.; Yang, X.; Wang, M.; Su, R.; He, Z. Rational Design of Chiral Nanostructures from Self-Assembly of a Ferrocene-Modified Dipeptide. *J. Am. Chem. Soc.* **2015**, *137*, 7869–7880. [CrossRef] [PubMed]
23. Xu, L.; Zhang, M.; Zhu, X.; Xue, C.; Wang, H.-X.; Liu, M. Solvent-Modulated Chiral Self-Assembly: Selective Formation of Helical Nanotubes, Nanotwists, and Energy Transfer. *ACS Appl. Mater. Interfaces* **2022**, *14*, 1765–1773. [CrossRef] [PubMed]
24. Yin, Y.-Y.; Cao, X.-C.; Cheng, P.; Ma, J.-G. Solvent Induced Conformational Transformation of Helical Chains in New Copper(II) Coordination Polymers. *Inorg. Chem. Commun.* **2012**, *24*, 7–10. [CrossRef]
25. Choi, H.; Cho, K.J.; Seo, H.; Ahn, J.; Liu, J.; Lee, S.S.; Kim, H.; Feng, C.; Jung, J.H. Transfer and Dynamic Inversion of Coassembled Supramolecular Chirality through 2D-Sheet to Rolled-Up Tubular Structure. *J. Am. Chem. Soc.* **2017**, *139*, 17711–17714. [CrossRef] [PubMed]
26. Li, P.; Lu, B.; Han, D.; Duan, P.; Liu, M.; Yin, M. Stoichiometry-controlled inversion of circularly polarized luminescence in co-assembly of chiral gelators with an achiral tetraphenylethylene derivative. *Chem. Commun.* **2019**, *55*, 2194–2197. [CrossRef]
27. Liu, G.; Sheng, J.; Wu, H.; Yang, C.; Yang, G.; Li, Y.; Ganguly, R.; Zhu, L.; Zhao, Y. Controlling Supramolecular Chirality of Two-Component Hydrogels by J- and H-Aggregation of Building Blocks. *J. Am. Chem. Soc.* **2018**, *140*, 6467–6473. [CrossRef]
28. Liu, G.-F.; Zhu, L.-Y.; Ji, W.; Feng, C.-L.; Wei, Z.-X. Inversion of the Supramolecular Chirality of Nanofibrous Structures through Co-Assembly with Achiral Molecules. *Angew. Chem. Int. Ed.* **2016**, *55*, 2411–2415. [CrossRef]
29. Martial, B.; Lefevre, T.; Buffeteau, T.; Auger, M. Vibrational Circular Dichroism Reveals Supramolecular Chirality Inversion of α-Synuclein Peptide Assemblies upon Interactions with Anionic Membranes. *ACS Nano* **2019**, *13*, 3232–3242. [CrossRef]
30. Wang, Y.; Li, Q.; Zhang, J.; Qi, W.; You, S.; Su, R.; He, Z. Self-Templated, Enantioselective Assembly of an Amyloid-like Dipeptide into Multifunctional Hierarchical Helical Arrays. *ACS Nano* **2021**, *15*, 9827–9840. [CrossRef]
31. Wu, A.; Guo, Y.; Li, X.; Xue, H.; Fei, J.; Li, J. Co-assembled Supramolecular Gel of Dipeptide and Pyridine Derivatives with Controlled Chirality. *Angew. Chem. Int. Ed.* **2021**, *60*, 2099–2103. [CrossRef] [PubMed]
32. Xu, H.; Lu, H.; Zhang, Q.; Chen, M.; Shan, Y.; Xu, T.-Y.; Tong, F.; Qu, D.-H. Surfactant-Induced Chirality Transfer, Amplification and Inversion in a Cucurbit[8]uril–Viologen Host–Guest Supramolecular System. *J. Mater. Chem. C* **2022**, *10*, 2763–2774. [CrossRef]
33. Go, M.; Choi, H.; Kim, K.Y.; Moon, C.J.; Choi, Y.; Miyake, H.; Lee, S.S.; Jung, S.H.; Choi, M.Y.; Jung, J.H. Temperature-Controlled Helical Inversion of Asymmetric Triphenylamine-Based Supramolecular Polymers; Difference of Handedness at the Micro- and Macroscopic Levels. *Org. Chem. Front.* **2019**, *6*, 1100–1108. [CrossRef]
34. Komori, H.; Inai, Y. Control of Peptide Helix Sense by Temperature Tuning of Noncovalent Chiral Domino Effect. *J. Org. Chem.* **2007**, *72*, 4012–4022. [CrossRef]
35. Bisoyi, H.K.; Li, Q. Light-Directed Dynamic Chirality Inversion in Functional Self-Organized Helical Superstructures. *Angew. Chem. Int. Ed.* **2016**, *55*, 2994–3010. [CrossRef] [PubMed]
36. Gopal, A.; Hifsudheen, M.; Furumi, S.; Takeuchi, M.; Ajayaghosh, A. Thermally Assisted Photonic Inversion of Supramolecular Handedness. *Angew. Chem. Int. Ed.* **2012**, *51*, 10505–10509. [CrossRef]

37. Koch, C.D.; Gladwin, M.T.; Freeman, B.A.; Lundberg, J.O.; Weitzberg, E.; Morris, A. Enterosalivary Nitrate Metabolism and the Microbiome: Intersection of Microbial Metabolism, Nitric Oxide and Diet in Cardiac and Pulmonary Vascular Health. *Free Radic. Biol. Med.* **2017**, *105*, 48–67. [CrossRef]
38. Xu, Y.; Pang, B.; Hu, L.; Feng, X.; Hu, L.; Wang, J.; Zhang, C.; Wang, S. Dietary Nitrate Protects Submandibular Gland from Hyposalivation in Ovariectomized Rats via Suppressing Cell Apoptosis. *Biochem. Biophys. Res. Commun.* **2018**, *497*, 272–278. [CrossRef]
39. Yang, Y.; Li, S.; Qu, Y.; Wang, X.; An, W.; Li, Z.; Han, Z.; Qin, L. Nitrate Partially Inhibits Lipopolysaccharide-Induced Inflammation by Maintaining Mitochondrial Function. *J. Int. Med. Res.* **2020**, *48*, 300060520902605. [CrossRef]
40. Lowenberg, C.; Julich-Gruner, K.K.; Neffe, A.T.; Behl, M.; Lendlein, A. Salt-Induced Shape-Memory Effect in Gelatin-Based Hydrogels. *Biomacromolecules* **2020**, *21*, 2024–2031. [CrossRef]
41. Yuan, J.; Zhang, Y.; Sun, Y.; Cai, Z.; Yang, L.; Lu, H. Salt- and pH-Triggered Helix-Coil Transition of Ionic Polypeptides under Physiology Conditions. *Biomacromolecules* **2018**, *19*, 2089–2097. [CrossRef] [PubMed]
42. Adamcik, J.; Mezzenga, R. Adjustable Twisting Periodic Pitch of Amyloid Fibrils. *Soft Matter* **2011**, *7*, 5437–5443. [CrossRef]
43. Hu, Y.; Lin, R.; Zhang, P.; Fern, J.; Cheetham, A.G.; Patel, K.; Schulman, R.; Kan, C.; Cui, H. Electrostatic-Driven Lamination and Untwisting of β-Sheet Assemblies. *ACS Nano* **2016**, *10*, 880–888. [CrossRef] [PubMed]
44. Drew, H.; Takano, T.; Tanaka, S.; Itakura, K.; Dickerson, R.E. High-Salt d(CpGpCpG), a Left-Handed Z′ DNA Double Helix. *Nature* **1980**, *286*, 567–573. [CrossRef] [PubMed]
45. Bukharina, D.; Kim, M.; Han, M.J.; Tsukruk, V.V. Cellulose Nanocrystals' Assembly under Ionic Strength Variation: From High Orientation Ordering to a Random Orientation. *Langmuir* **2022**, *38*, 6363–6375. [CrossRef]
46. Chen, M.; Huang, Y.; Lee, S.C. Salt-assisted Synthesis of Hollow $Bi_2WO_6$ Microspheres with Superior Photocatalytic Activity for NO Removal. *Chin. J. Catal.* **2017**, *38*, 348–356. [CrossRef]
47. Hosono, E.; Fujihara, S.; Kakiuchi, K.; Imai, H. Growth of Submicrometer-Scale Rectangular Parallelepiped Rutile $TiO_2$ Films in Aqueous $TiCl_3$ Solutions under Hydrothermal Conditions. *J. Am. Chem. Soc.* **2004**, *126*, 7790–7791. [CrossRef]
48. Liu, X.; Jin, Z.; Bu, S.; Zhao, J.; Liu, Z. Growth of ZnO Films with Controlled Morphology by Aqueous Solution Method. *J. Am. Ceram. Soc.* **2006**, *89*, 1226–1231. [CrossRef]
49. Yin, B.; Zhou, W.; Long, Q.; Li, C.; Zhang, Y.; Yao, S. Salt-assisted Rapid Transformation of $NaYF_4$:$Yb^{3+}$,$Er^{3+}$ Nanocrystals from Cubic to Hexagonal. *CrystEngComm* **2014**, *16*, 8348–8355. [CrossRef]
50. Xu, Y.; Bao, S.-S.; Huang, X.-D.; Zheng, L.-M. Homochiral Erbium Coordination Polymers: Salt-Assisted Conversion from Triple to Quadruple Helices. *Cryst. Growth Des.* **2018**, *18*, 4045–4053. [CrossRef]
51. Huang, J.; Ding, H.-M.; Xu, Y.; Zeng, D.; Zhu, H.; Zang, D.-M.; Bao, S.-S.; Ma, Y.-Q.; Zheng, L.-M. Chiral Expression from Molecular to Macroscopic Level via pH Modulation in Terbium Coordination Polymers. *Nat. Commun.* **2017**, *8*, 2131. [CrossRef] [PubMed]
52. Wu, L.-Q.; Xu, Y.; Hou, T.; Jia, J.-G.; Huang, X.-D.; Weng, G.-G.; Bao, S.-S.; Zheng, L.-M. Controllable Macroscopic Chirality of Coordination Polymers through pH and Anion-Mediated Weak Interactions. *Chem. Eur. J.* **2021**, *27*, 16722–16734. [CrossRef] [PubMed]
53. Kang, S.O.; Begum, R.A.; Bowman-James, K. Amide-Based Ligands for Anion Coordination. *Angew. Chem. Int. Ed.* **2006**, *45*, 7882–7894. [CrossRef] [PubMed]
54. Mihaylov, M.Y.; Zdravkova, V.R.; Ivanova, E.Z.; Aleksandrov, H.A.; Petkov, P.S.; Vayssilov, G.N.; Hadjiivanov, K.I. Infrared Spectra of Surface Nitrates: Revision of the Current Opinions Based on the Case Study of Ceria. *J. Catal.* **2021**, *394*, 245–258. [CrossRef]
55. Morozov, I.V.; Serezhkin, V.N.; Troyanov, S.I. Modes of Coordination and Stereochemistry of the $NO_3^-$ Anions in Inorganic Nitrates. *Russ. Chem. Bull.* **2008**, *57*, 439–450. [CrossRef]
56. Wu, J.-Y.; Liu, Y.-C.; Chao, T.-C. From 1D helix to 0D Loop: Nitrite Anion Induced Structural Transformation Associated with Unexpected N-Nitrosation of Amine Ligand. *Inorg. Chem.* **2014**, *53*, 5581–5588. [CrossRef] [PubMed]
57. Langton, M.J.; Duckworth, L.C.; Beer, P.D. Nitrate Anion Templated Assembly of a [2]Rotaxane for Selective Nitrate Recognition in Aqueous Solvent Mixtures. *Chem. Commun.* **2013**, *49*, 8608–8610. [CrossRef]
58. Siddiqui, K.A.; Mehrotra, G.K.; Mrozinski, J.; Butcher, R.J. Anion Assisted Self-Assembly of a Ni(II) Complex into Metallo-Supramolecular Network Involving H-bonded Synthons as Nodes. *J. Mol. Struct.* **2010**, *964*, 18–26. [CrossRef]
59. Xie, T.-Z.; Guo, C.; Yu, S.-Y.; Pan, Y.-J. Fine-Tuning Conformational Motion of a Self-Assembled Metal-Organic Macrocycle by Multiple C-H·Anion Hydrogen Bonds. *Angew. Chem. Int. Ed.* **2012**, *51*, 1177–1181. [CrossRef]
60. Zhou, L.-P.; Sun, Q.-F. A self-assembled Pd2L4 cage that selectively encapsulates nitrate. *Chem. Commun.* **2015**, *51*, 16767–16770. [CrossRef]
61. TOPAS. *Version 5.0*; Bruker AXS Inc.: Madison, WI, USA, 2014.
62. Liu, X.-G.; Bao, S.-S.; Huang, J.; Otsubo, K.; Feng, J.-S.; Ren, M.; Hu, F.-C.; Sun, Z.-H.; Zheng, L.-M.; Wei, S.-Q.; et al. Homochiral metal phosphonate nanotubes. *Chem. Commun.* **2015**, *51*, 15141–15144. [CrossRef] [PubMed]
63. Weng, G.-G.; Hong, B.-K.; Bao, S.-S.; Wen, Y.; Wu, L.-Q.; Huang, X.-D.; Jia, J.-G.; Wen, G.-H.; Li, S.-H.; Peng, L.; et al. From Helices to Superhelices: Hierarchical Assembly of Homochiral van der Waals 1D Coordination Polymers. *Chem. Sci.* **2021**, *12*, 12619–12630. [CrossRef] [PubMed]

64. Liu, X.-G.; Bao, S.-S.; Li, Y.-Z.; Zheng, L.-M. Polymorphism in Homochiral Zinc Phosphonates. *Inorg. Chem.* **2008**, *47*, 5525–5527. [CrossRef] [PubMed]
65. SAINT. *Version 8.40 A, Program for Data Extraction and Reduction*; Bruker Nano Inc.: Madison, WI, USA, 2019.
66. SHELXT 2014/5, Sheldrick, 2014; SHELXL 2018/3, Sheldrick, 2018. Available online: http://shelx.uni-goettingen.de/ (accessed on 1 March 2018).